Publ. Astron. Soc. Japan (2020) 72 (4), 57 (1–13)
doi: 10.1093/pasj/psaa024
Advance Access Publication Date: 2020 May 27

Trigonometric parallax of O-rich Mira variable star OZ Gem (IRAS 07308+3037): A confirmation of the difference between the P–L relations of the Large Magellanic Cloud and the Milky Way

Riku URAGO,[1,*] Ryohei YAMAGUCHI,[1] Toshihiro OMODAKA,[1] Takumi NAGAYAMA,[2] James O. CHIBUEZE,[3,4] Masayuki Y. FUJIMOTO,[5] Takahiro NAGAYAMA,[1] Akiharu NAKAGAWA,[1] Yuji UENO,[2] Miho KAWABATA,[6,7] Tatsuya NAKAOKA,[7] Kengo TAKAGI,[7,8] Masayuki YAMANAKA,[7,9] and Koji KAWABATA[7]

[1]Department of Physics and Astronomy, Graduate School of Science and Engineering, Kagoshima University, 1-21-35 Korimoto, Kagoshima, Kagoshima 890-0065, Japan
[2]Mizusawa VLBI Observatory, National Astronomical Observatory of Japan, 2-21-1 Osawa, Mitaka, Tokyo 181-8588, Japan
[3]Centre for Space Research, Physics Department, North-West University, Potchefstroom 2520, South Africa
[4]Department of Physics and Astronomy, Faculty of Physical Sciences, University of Nigeria, Carver Building, 1 University Road, Nsukka, Nigeria
[5]Department of Physics, Hokkaido University, Sapporo, Hokkaido 060-0810, Japan
[6]Department of Astronomy, Kyoto University, Kitashirakawa-Oiwakecho, Sakyo-ku, Kyoto, Kyoto 606-8502, Japan
[7]Hiroshima Astrophysical Science Center, Hiroshima University, Higashi-Hiroshima, Hiroshima 739-8526, Japan
[8]School of Science, Graduate School of Science, Hiroshima University, Higashi-Hiroshima, Hiroshima 739-8526, Japan
[9]Okayama Observatory, Kyoto University, 3037-5 Honjo, Kamogata-cho, Asakuchi, Okayama 719-0232, Japan

*E-mail: k4841512@kadai.jp

Received 2019 October 15; Accepted 2020 March 6

Abstract

OZ Geminorum (OZ Gem) is a galactic Mira variable in the Milky Way (MW). We measured its annual parallax with VLBI Exploration of Radio Astrometry to be $\pi = 0.806 \pm 0.039$ mas, corresponding to a distance of $D = 1.24 \pm 0.06$ kpc. Based on multi-epoch infrared observations with the Kagoshima University 1 m telescope, we also derived the mean *J*-, *H*-, and *K*′-band magnitudes of OZ Gem to be 5.75 ± 0.47 mag, 4.00 ± 0.16 mag, and 2.65 ± 0.16 mag, respectively. We derived a pulsation period of OZ Gem as 592 ± 1 d from the *K*′-band lightcurve. From the period–luminosity (P–L) relation and two-color diagram of the Large Magellanic Cloud (LMC), the property of OZ Gem suggests that

OZ Gem is assigned among the carbon-rich Mira variables. However, our optical spectroscopic observational results (with the 1.5 m Kanata telescope) confirmed OZ Gem to be an oxygen-rich Mira star with the detection of multiple titanium oxide transition absorption lines. We suggest that OZ Gem is a low-mass star evolving to an OH/IR star with large mass loss and dust formation. It is predicted that the lower limit to the initial mass of AGB stars for developing the C-rich surface chemistry is larger in the MW than in the LMC because of larger metallicity, and OZ Gem is likely to be the first example to prove this. Our results highlight the necessity of deriving the PL relation of the Milky Way with high accuracy.

Key words: astrometry — masers (H_2O) — stars: AGB and post-AGB — stars: individual (OZ Gem [IRAS 07308+3037])

1 Introduction

Understanding the nature of the Milky Way and reconstructing its map have been the aim of many observational projects at various wavelengths in the last decade. While Hipparcos (HIgh Precision PARallax COllecting Satellite) and Gaia have both produced significant numbers of parallaxes of stars in the Milky Way (van Leeuwen 2007; Gaia Collaboration 2018), very long baseline interferometry (VLBI) astrometric projects like the Bar and Spiral Structure Legacy (BeSSeL) Survey and VLBI Exploration of Radio Astrometry (VERA) have provided fewer but more accurate parallaxes to maser sources in the Milky Way (Honma et al. 2012; Reid et al. 2014). However, most of the VLBI astrometric results are dominantly toward star-forming regions located in the spiral arms of the Milky Way.

The relationship between the K'-band absolute magnitude (M_K) and the logarithm of the pulsation period (log P) of a Mira variable is well constrained for the Large Magellanic Cloud (LMC; see Feast et al. 1989; Ita et al. 2004), and serves as a distance indicator. The M_K–log P relation of the LMC cannot be adopted for the Milky Way because the metallicity of the Milky Way is twice that of the LMC (Luck et al. 1998), thus the need to derive the M_K–log P relation peculiar to the Milky Way. This task can be daunting due to the high uncertainty in the distance estimates which introduce significantly large errors in the M_K values. Deriving accurate distances to asymptotic giant branch (AGB) stars with VLBI astrometric techniques is one way to constrain the M_K–log P relation of the Milky Way and compare it to that of the LMC.

OZ Gem (also known as IRAS 07308+3037) is an M9.5 star (Solf 1978) associated with maser emission of water (H_2O) and silicon oxide (SiO) $v = 1$ and $v = 2$ transitions (Kim et al. 2014). Gaia Data Release 2 (DR2) reported the G-band mean magnitude of OZ Gem to be 13.7 and its effective temperature ($T_{\rm eff}$) to be 3280.5 K (Gaia Collaboration 2018). There is no information in the literature on any previous distance measurement toward OZ Gem. The General Catalog of Variable Stars (GCVS) contains no information about the period of OZ Gem.

In this paper we report on the first parallax-distance measurement through VERA phase-referenced observations of the H_2O masers associated with OZ Gem. Since OZ Gem is mostly invisible in the optical, we set out to determine its pulsation period by conducting multi-epoch J-, H-, and K'-band observations of OZ Gem using the Kagoshima University 1 m optical/infrared telescope. The results of our VERA and infrared observations, along with those of the spectroscopic observations with the 1.5 m Kanata telescope at Higashi-Hiroshima Observatory, are discussed in this paper.

2 Observations

2.1 VERA observations

The VLBI monitoring observations of 22.235080 GHz H_2O (6_{16}–5_{23}) masers of OZ Gem were made with VERA at 20 epochs from 2013 to 2015. The observation dates (year/current day) were 2013/034, 2013/061, 2013/095, 2013/143, 2013/237, 2013/285, 2013/309, 2013/335, 2014/020, 2014/031, 2014/094, 2014/133, 2014/166, 2014/287, 2014/320, 2014/331, 2014/356, 2015/032, 2015/086, and 2015/122. Since the H_2O maser of OZ Gem was not detected in 2013/237, we used the other 19 epochs to measure the parallax. To measure the absolute positions of the masers in OZ Gem, a position reference source, J0741+3112 listed in the second realization of the International Celestial Reference Frame (ICRF 2) catalogue, was simultaneously observed with the VERA dual beam system. The separation angle between the two sources is 1.°7.

The data correlation process was performed with the Mitaka FX-type hardware correlator (Chikada et al. 1991) for the 2013–2014 observations and the Mizusawa FX-type software correlator (Oyama et al. 2016) for the 2015 observations. The phase tracking centers of OZ Gem and J0741+3112 were set at

$(\alpha, \delta)_{J2000.0}$ = ($07^h33^m57^s.7500$, $+30^\circ30'37''.799$) and ($07^h41^m10^s.703308$, $+31^\circ12'00''.22917$), respectively. The frequency bandwidth and spacing for OZ Gem were 16 MHz and 31.25 kHz, corresponding to a velocity coverage of 215 km s^{-1} and velocity spacing of 0.42 km s^{-1}, respectively. The frequency bandwidth and spacing for J0741+3112 were 16 MHz × 15 IFs = 240 MHz and 250 kHz, respectively.

The data reduction was performed with the Astronomical Image Processing System (AIPS) developed by the National Radio Astronomy Observatory (NRAO). The amplitude was calibrated using the gain curve and the system noise temperature, measured during the observations with the `RSky` package. The absolute positions of the masers in OZ Gem were measured with respect to J0741+3112 using phase-referencing calibration. The fringe search for J0741+3112 was done with an integration time of 60 s and a time interval of 30 s. Self-calibration of J0741+3112 was also done to calibrate the phase variation caused by the structure of this source. The solutions obtained by the fringe search and the self-calibration of J0741+3112 were applied to OZ Gem.

The instrumental delay between the dual beams was calibrated by the horn-on-dish method, in which artificial noise sources are mounted on the antenna feedome base and wide-band radio noise is injected into the dual-beam receivers after reflection by a subreflector (Honma et al. 2008a). The troposphere delay was calibrated using the troposheric zenith delay measured with GPS (Honma et al. 2008b) and the Niell mapping function (Niell 1996). The ionospheric delay was corrected based on the Global Ionosphere Map (GIM) produced by the University of Bern.

After the phase-referencing calibration, the visibility of OZ Gem was Fourier transformed to the dirty image and was CLEANed. From the CLEAN map, the position, the peak intensity, and the image dynamic range of the maser spots were obtained. The detection criterion was an image dynamic range higher than seven. The synthesized beam size of the phase-referencing image was typically 1.47 mas × 0.80 mas with a position angle of -55°.

2.2 Infrared observations with the Kagoshima University 1 m telescope

We performed near-infrared (NIR) monitoring observations of OZ Gem between 2004 to 2016 using the Kagoshima University 1 m telescope. The near-infrared camera equipped on the telescope has a 512 × 512 pixel HAWAII array, which provides the *J*-, *H*-, and *K*′-band images. The image scale of the array is 0.636 pixel, yielding a field of view of $5'.025 \times 5'.025$. The data reduction and photometry for these data were carried out using the National Optical Astronomy Observatory Imaging Reduction and Analysis Facility (IRAF) software package. Standard procedures for near-infrared array image reduction were adopted. The average dark frame was subtracted, normalizing each of the dark-subtracted images by the flat-field frame. Subsequently, the sky frame was subtracted from the normalized image. The photometry was carried out with the IRAF/APPHOT package. Since OZ Gem is too bright in the near-infrared and causes saturation of the detector, we used two observation modes: the image-defocus technique between 2004 and 2013 for all bands, and a technique using the Local Attenuation Filter (LAF) between 2014 and 2016 for the *K*′ band only. LAF was originally developed for the InfraRed Survey Facility (IRSF) 1.4 m telescope for the observation of very bright NIR stars (Nagayama 2016) and was also installed on the Kagoshima University 1 m telescope (T. Nagayama et al. in preparation).

2.3 Spectroscopic observations with the 1.5 m Kanata telescope

A Mira variable star can be C-rich or O-rich. The dominant spectral feature of C-rich AGB stars is the presence of carbon nitride (CN) absorption features, while O-rich AGB stars show dominant titanium oxide (TiO) absorption features (Guglielmo et al. 1997). To test the richness of carbon and oxygen in OZ Gem, we carried out spectroscopic observations of OZ Gem on 2017 December 1 and 2 with the Hiroshima One-shot Wide-field Polarimeter (HOWPol; Kawabata et al. 2008) attached to the 1.5 m Kanata telescope at Higashi-Hiroshima Observatory. We used a $2''.3$ width slit and a 420 lines mm^{-1} grism, which give a wavelength coverage of 4500–9200 Å and a wavelength dispersion of $R = \lambda/\Delta\lambda \simeq 400$ with a wavelength error of $\simeq 3.5$ Å. The flux scale was calibrated with the data of the spectrophotometric standard star HR 1544 obtained just after the observation of OZ Gem with the same optical setting.

3 Results

3.1 Annual parallax and maser internal motion

Figure 1 shows the self-calibration map of the position reference source, J0741+3112. Two components separated by 2.7 mas in the north–south direction were detected. The peak intensities of the north and south components are 0.6 Jy beam^{-1} and 0.4 Jy beam^{-1}, respectively. The 2.3 GHz and 8.4 GHz continuum images with the global VLBI array including the Very Long Baseline Array (VLBA) and European VLBI Network (EVN) show the jet-like

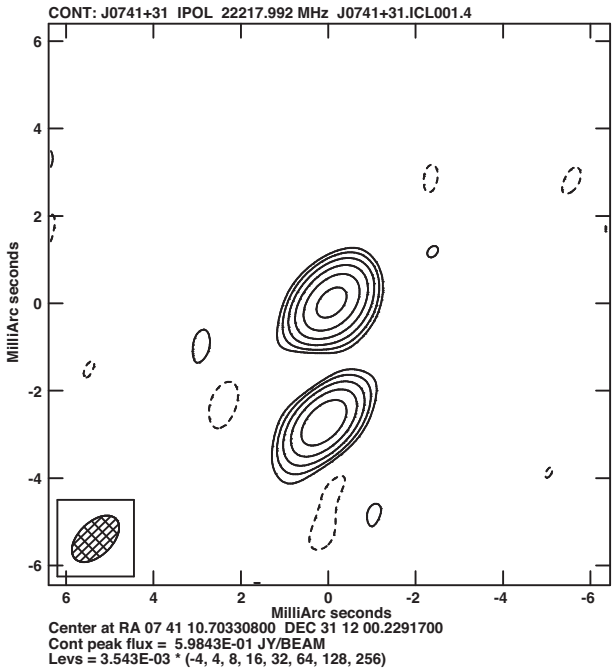

Fig. 1. Self-calibration map of the position reference source, J0741+3112, at the first epoch. The contour levels are −4, 4, 8, 16, 32, 64, and 128 σ, where σ is 3.54 mJy beam^{-1}.

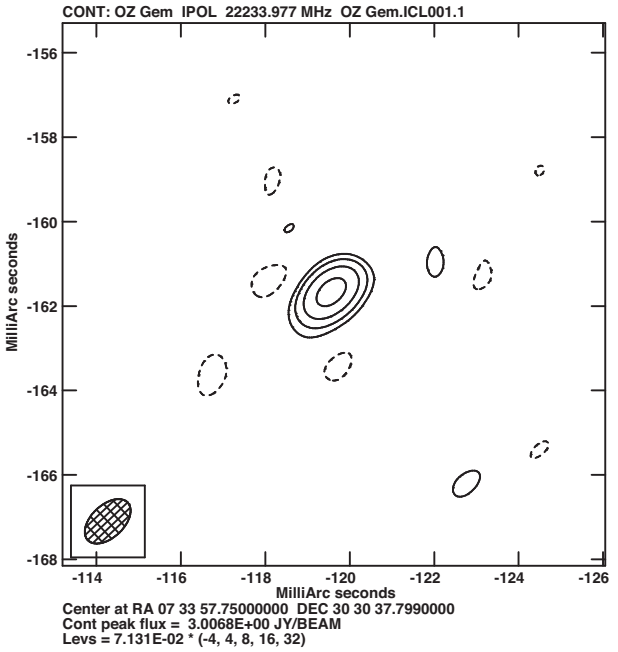

Fig. 2. Phase-referencing map of the H_2O maser spot at v_{LSR} = 12.00 km s^{-1} in OZ Gem at the first epoch. The contour levels are −4, 4, 8, 16, and 32 σ, where σ is 71.3 mJy beam^{-1}.

structure elongated from the core to the south direction (Pushkarev & Kovalev 2012). Our image of J0741+3112 appears to trace a similar structure, as shown in figure 1, with two (north and south) components. Since the two components were stable and their structures did not change, they did not affect our parallax measurement. Figure 2 shows the phase-referencing map of the H_2O maser spot at the local standard of rest (LSR) velocity $v_{LSR} = 12.0$ km s^{-1} in OZ Gem. This spot is an isolated point-like spot with no prominent structure and is detected for all observations. Therefore we used this spot to measure the parallax.

The parallax of OZ Gem was obtained to be $\pi = 0.806 \pm 0.039$ mas, corresponding to a distance of $D = 1.24 \pm 0.06$ kpc. This parallax was obtained to fit the positional variations of the maser spot at $v_{LSR} = 12.00$ km s^{-1} with five fitting parameters of the parallax: π, the proper motion ($\mu_\alpha \cos\delta$, μ_δ), and the position offset ($\Delta\alpha\cos\delta$, $\Delta\delta$). The fitting result is shown in figure 3. In this fitting, the positional errors of each epoch calculated by $\sigma_{tot} = \sqrt{\sigma_{ran}^2 + \sigma_{sys}^2}$ were applied, and they are shown as the error bars in figure 3. The random errors caused by the thermal noise were calculated to be $\sigma_{ran} = \theta_{beam}/(2SNR) = 0.011$–$0.074$ mas, where θ_{beam} is the synthesized beam size and SNR is the image dynamic range of the phase-referencing map. The systematic errors, which are caused by the uncalibrated delay errors such as the tropospheric delay error and the structural effects of both maser and reference sources, were estimated to be ($\sigma_{sys,\alpha}$, $\sigma_{sys,\delta}$) = (0.115, 0.115) mas to achieve a reduced χ^2 value of unity for the parallax fitting. The fitting residuals were calculated to be ($\sigma_{res,\alpha}$, $\sigma_{res,\delta}$) = (0.119, 0.121) mas. This indicates that the positional error caused by the structural effect of J0741+3112 would be less than 0.12 mas. Gaia DR2 attempted to derive the parallax for OZ Gem. However, they could not measure the parallax correctly because it seems that the photcentric position of Mira variables moves around significantly.

The absolute proper motions of 22 maser spots detected over three epochs were measured. They are listed in table 1, and their distributions are shown in figure 4. Since the systematic proper motion is common for all the spots and the internal motions of the masers are different for the individual spots, the average and the residuals should give the stellar motion of OZ Gem and the internal motions of the spots. The average of the absolute proper motions is obtained to be ($\overline{\mu}_\alpha \cos\delta$, $\overline{\mu}_\delta$) = (-1.97 ± 0.32, -8.69 ± 0.21) mas yr^{-1}. The error is the standard error. The residual vectors indicating the internal motions are shown in figure 4. The H_2O maser spots are distributed with an area of 43 mas × 46 mas (54 au × 57 au at 1.24 kpc). The blue- and red-shifted spots are seen at the northeast and southwest sides, respectively, and expand from each other at the internal motion velocity of approximately 2 mas yr^{-1} (12 km s^{-1} at 1.24 kpc).

The LSR velocity range of the detected H_2O maser spots is from −1.48 to 16.21 km s^{-1}. Their average is obtained to be $v_{LSR} = 8.7 \pm 1.4$ km s^{-1} and is close to the stellar

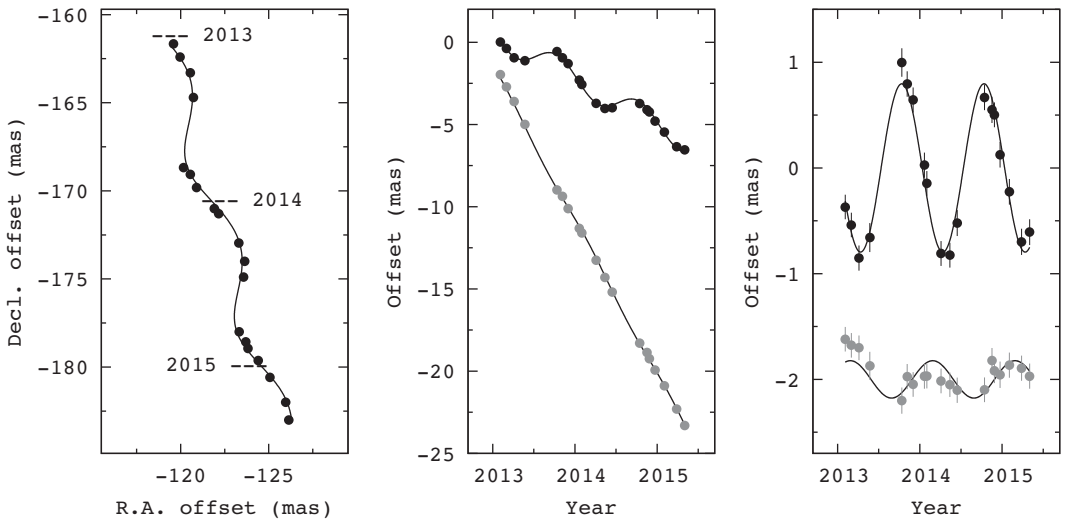

Fig. 3. Parallax and proper motion data and fits of the H_2O maser spot at $v_{LSR} = 12.00\,km\,s^{-1}$ in OZ Gem. The solid line shows the best-fitting results of parallax and proper motion. Left panel: Positions on the sky. Middle panel: RA (black circle) and Dec (gray circle) offset versus time. Right panel: Same as the middle panel, except the proper motion has been removed, allowing the effect of only the parallax to be seen.

Table 1. Position offsets ($\Delta\alpha\cos\delta$, $\Delta\delta$), the absolute proper motions ($\mu_\alpha\cos\delta$, μ_δ), and the LSR velocities (v_{LSR}) of H_2O maser spots in OZ Gem.*

No.	$\Delta\alpha\cos\delta$ (mas)	$\Delta\delta$ (mas)	$\mu_\alpha\cos\delta$ (mas yr^{-1})	μ_δ (mas yr^{-1})	v_{LSR} (km s^{-1})
1	−124.81	−152.56	−3.55 ± 2.47	−8.60 ± 2.35	14.53
2	−123.13	−173.10	−2.33 ± 0.18	−9.33 ± 0.17	11.58
3	−121.00	−170.59	−5.33 ± 0.49	−8.81 ± 0.42	11.16
4	−120.30	−169.51	−5.63 ± 0.60	−7.06 ± 0.55	12.42
5	−119.36	−162.21	−2.44 ± 0.06	−9.00 ± 0.06	12.42
6	−119.22	−162.04	−2.82 ± 0.05	−9.38 ± 0.05	12.00
7	−119.17	−162.26	−2.57 ± 0.21	−9.54 ± 0.21	11.58
8	−119.10	−162.76	−1.17 ± 3.21	−10.73 ± 3.10	11.16
9	−118.97	−171.00	−1.59 ± 0.42	−8.93 ± 0.36	13.26
10	−118.32	−160.41	−2.00 ± 1.57	−9.90 ± 1.38	12.42
11	−118.14	−160.35	−0.71 ± 0.13	−9.17 ± 0.12	12.84
12	−116.49	−128.03	−1.89 ± 0.87	−6.89 ± 0.76	−0.64
13	−116.51	−128.57	−2.18 ± 0.63	−6.94 ± 0.62	−1.48
14	−116.22	−127.17	−1.98 ± 0.25	−7.21 ± 0.23	−1.06
15	−113.34	−140.83	−1.61 ± 0.32	−8.01 ± 0.28	16.21
16	−112.97	−139.33	−1.37 ± 0.28	−8.43 ± 0.26	15.79
17	−112.12	−170.25	−2.52 ± 2.56	−8.22 ± 2.38	15.37
18	−111.97	−167.94	−1.82 ± 0.69	−10.01 ± 0.66	14.95
19	−84.52	−137.40	−1.24 ± 1.87	−8.66 ± 1.60	−0.22
20	−82.51	−138.24	1.09 ± 1.56	−9.57 ± 1.45	−0.64
21	−81.82	−138.35	0.28 ± 0.12	−8.31 ± 0.12	−1.06
22	−81.38	−138.26	0.06 ± 0.17	−8.40 ± 0.15	−1.48

*The position offsets are with respect to the phase-tracking center, $(\alpha, \delta)_{J2000.0} = (07^h33^m57\overset{s}{.}7500, +30°30'37\overset{''}{.}799)$.

velocity of OZ Gem, which is expected to be $v_{LSR} = 7\,km\,s^{-1}$ (Benson et al. 1990; Kim et al. 2013) from the average of the blue- and red-shifted components detected for the previous H_2O maser observations (Zuckerman & Lo 1987). The LSR velocities of SiO $v = 1$ and $v = 2$ masers are 4.3 and 4.5 km s^{-1}, respectively (Kim et al. 2013). These velocities are within the LSR velocity range of the H_2O masers.

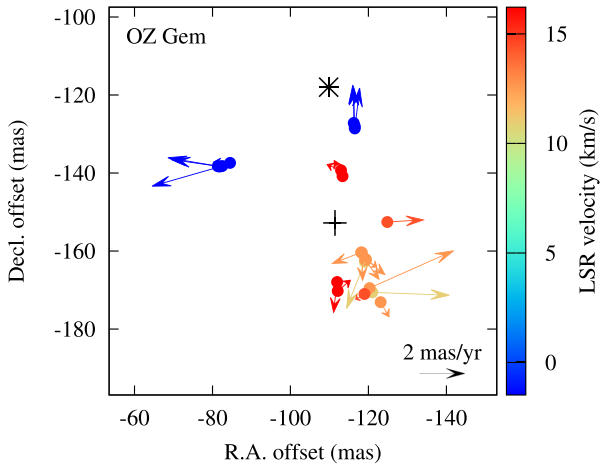

Fig. 4. Distributions and internal motions of the H_2O maser spots in OZ Gem. The origin (0,0) mas is the phase-tracking center, $(\alpha, \delta)_{J2000.0} = (07^h33^m57^s.7500, +30°30'37''.799)$. The vector of 2 mas yr^{-1} at the bottom right corner corresponds to 11.8 km s^{-1} at the distance of 1.24 kpc. The cross shows the central position of the H_2O maser spot distribution. The asterisk shows the stellar position expected from Gaia DR2 (Gaia Collaboration 2018). (Color online)

The absolute proper motion of OZ Gem is measured to be $(\mu_\alpha \cos\delta,\ \mu_\delta) = (0.489 \pm 0.699,\ -10.867 \pm 0.592)$ mas yr^{-1} by Gaia DR2 (Gaia Collaboration 2018), although the parallax has not yet been measured. The average absolute proper motion of the masers is $(\overline{\mu}_\alpha \cos\delta, \overline{\mu}_\delta) = (-1.97 \pm 0.32, -8.69 \pm 0.21)$ mas yr^{-1}. The difference is $(-2.46 \pm 0.77,\ 2.18 \pm 0.63)$ mas yr^{-1}, corresponding to a velocity of $(-15 \pm 5,\ 13 \pm 4)$ km s^{-1} at $D = 1.24$ kpc. The central position of the H_2O maser is calculated to be $(\Delta\alpha\cos\delta, \Delta\delta) = (-111.4 \pm 3.0, -152.8 \pm 3.3)$ mas. The stellar position estimated by Gaia DR2 is $(\Delta\alpha\cos\delta, \Delta\delta) = (-109.8 \pm 0.3, -118.0 \pm 0.4)$ mas. Their positions are shown in figure 4. There is an offset of $(-1.6 \pm 3.0, -34.8 \pm 3.4)$ mas. The possible origin of this offset is discussed in subsection 4.4.

3.2 Photometry, spectroscopy, and light curve of OZ Gem

Table 2 shows the J-, H-, and K'-band magnitudes obtained for all the observation epochs. We obtained the light curve of OZ Gem as shown in figure 5. Using the J-, H-, and K'-band data, we solved for the period P by assuming a sinusoidal function of

$$m = m_0 + A \sin[2\pi(t + \theta)/P], \quad (1)$$

where m is the apparent magnitude, m_0 the averaged magnitude, A the amplitude, t the MJD, and θ the voluntary phase. From NIR observations, we obtained the mean J-, H-, and K'-band magnitude of OZ Gem to be 5.75 ± 0.47 mag, 4.00 ± 0.16 mag, and 2.65 ± 0.16 mag, respectively. The pulsation period of OZ Gem is 592 ± 1 d using the K' band, and 575 ± 11 d and 579 ± 5 d for the J and H bands respectively. The errors in the derived periods were obtained from the least squares fitting. Gaia DR2 reported the pulsation period for OZ Gem to be 588 d. This is consistent with our results. Note that the light curve of OZ Gem from Gaia DR2 is only derived from one cycle.

Figure 6 shows the position of OZ Gem (filled circle) in the M_K–log P relation of Nakagawa et al. (2016) using Mira variables in the Milky Way with an accurately measured distance.

Figure 7 shows our spectrum for OZ Gem. The TiO absorption features that characterize O-rich Mira variables are dominant in the spectra. The CN features that characterize C-rich Mira stars are not seen in the spectra, confirming OZ Gem to be an O-rich Mira variable star.

4 Discussion

4.1 OZ Gem: Properties and O-rich confirmation

Exploring the physical photometric properties of OZ Gem, we have derived the absolute bolometric magnitude (M_{bol}), luminosity (L), effective temperature (T_{eff}), initial mass (M), and radius (R) of OZ Gem. First, we determined the $V - K$ color, and used the $V - K$ values to estimate T_{eff} and BC_K from effective temperature versus $(V - K)$ and BC_K versus $(V - K)$ diagrams shown in Buzzoni et al. (2010), respectively.

With the average V-band magnitude of OZ Gem obtained from The International Variable Star Index (VSX)[1] and the K-band magnitude from our NIR observations, we get the mean V band and $(V - K)$ to be 12.21 and 9.56 mag, respectively. Based on Buzzoni et al. (2010), T_{eff} and BC_K for OZ Gem correspond to 3226 ± 207 K and 3.16 ± 0.18 mag, respectively.

The bolometric magnitude (M_{bol}) of OZ Gem can be computed from BC_K using $M_{bol} = BC_K + m_K$; we obtained M_{bol} to be 5.81 mag. The absolute bolometric magnitude (M_{bol}) of OZ Gem can be computed from M_{bol} using $M_{bol} = M_{bol} - 5 * \log 10(D/10)$, where D is the distance: we obtained M_{bol} to be -4.65. We derived the luminosity of OZ Gem using $M_{bol} - M_{bol\odot} = -2.5 * \log(L/L_\odot)$. Since $M_{bol\odot}$ is 4.74 (Torres 2010), $M_{bol} = 4.74 - 2.5 * \log(L/L_\odot)$. We obtained the luminosity to be $\log(L/L_\odot) = 3.76 \pm 0.13$.

To derive the radius of OZ Gem, we used $M_{bol} = 4.74 - 2.5 * \log 10(T_{eff}^4 * R^2 / T_{eff\,sun}^2 * R_{sun}^2)$ from Bessell, Castelli, and Plez (1998), and obtained $270 \pm 29\ R_\odot$ (the error in R propagated from the errors in the V- and K-band magnitudes).

[1] ⟨https://www.aavso.org/vsx/⟩.

Table 2. Epoch of near-infrared observations.

MJD	J (mag)	ΔJ (mag)	H (mag)	ΔH (mag)	K (mag)	ΔK (mag)	def/LAF*
53244	3.19	0.04	4.74	0.04	2.18	0.01	def
53281	3.2	0.05	4.73	0.07	2.18	0.03	def
53307	3.36	0.06	*5*	0.07			def
53327	3.6	0.1	5.26	0.17	2.56	0.02	def
53340			3.62	0.19			def
53354					2.72	0.02	def
53407	4.43	0.09	6.21	0.15	3.15	0.04	def
53437	4.67	0.1	6.57	0.13	3.32	0.09	def
53469	4.82	0.05	6.71	0.09	3.44	0.01	def
53495	5.03	0.09	6.93	0.09	3.73	0.05	def
54115					3.35	0.05	def
54170	*4.5*	0.23	7.15	0.12			def
54202	4.05	0.04	5.84	0.05	2.8	0.02	def
54229					2.51	0.02	def
54437			4.84	0.03	2.15	0.02	def
54474					2.31	0.02	def
54510			5.29	0.05			def
54525	3.75	0.05	*5.5*	0.05	2.68	0.02	def
54785					3.21	0.05	def
54818					2.62	0.06	def
54819	3.82	0.02	*5.5*	0.05	2.62	0.03	def
54872	3.38	0.05	5.02	0.06			def
54932					2.1	0.02	def
54950	3.19	0.01	4.87	0.02	2.09	0.03	def
54970	3.28	0.02	5.04	0.05	2.32	0.02	def
55656	3.72	0.03					def
55678	4.16	0.01	5.26	0.08			def
55913	4.87	0.08	6.78	0.06			def
56593					2.67	0.02	def
56613					2.4	0.01	def
56632					2.16	0.02	def
56660					2.13	0.01	def
56663					2.07	0.06	def
56680					2.01	0.01	def
56710					1.92	0.02	def
56723					1.93	0.01	def
56754					1.71	0.06	def
56791					2.06	0.07	def
56801					1.91	0	def
56974					2.89	0.22	LAF
56985					3.28	0.16	LAF
57026					3.34	0.12	LAF
57030					3.02	0.08	LAF
57047					3.4	0.11	LAF
57055					3.3	0.08	LAF
57136					3.24	0.16	LAF

*Where image defocus or local attenuation filter techniques were applied is indicated by def and LAF, respectively.

4.2 Period–luminosity relation: LMC vs. Milky Way

From the P–L relation of Mira variables of the Milky Way (figure 6), OZ Gem is observed to be dimmed by ∼1 mag from the extrapolation line. This is because OZ Gem has a large circumstellar dust envelope. The NIR color of OZ Gem, $H - K' = 1.35 \pm 0.05$ and $J - H = 1.75$ (see figure 8), is more reddened than the general Mira intrinsic

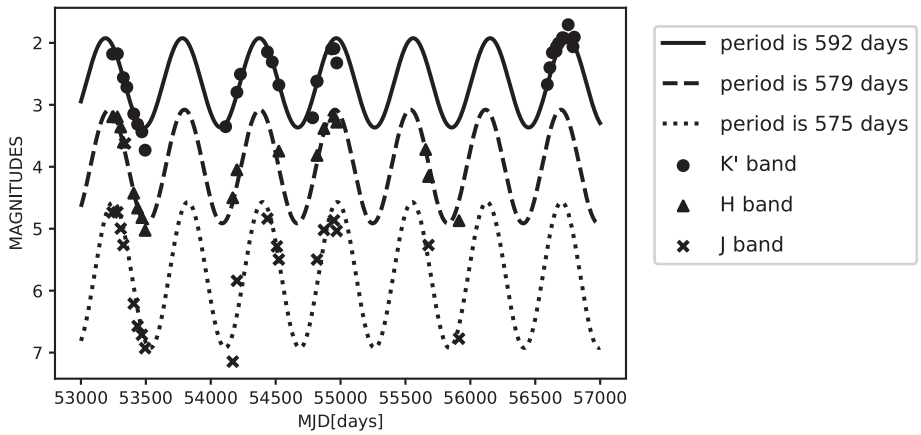

Fig. 5 Infrared *J*-, *H*-, and *K*′-band light curves of OZ Gem. The crosses, filled triangles, and filled circles represent the *J*, *H*, and *K*′ bands, respectively.

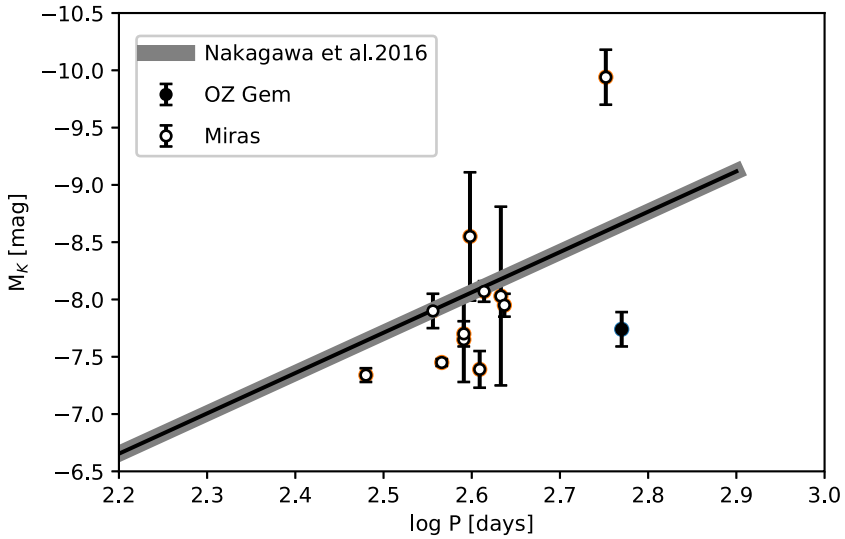

Fig. 6. M_K–log P relation of Nakagawa et al. (2016) using Mira variables in the Milky Way. Open circles are Mira variables and the filled circle represents OZ Gem. (Color online)

color (Mira box: Feast et al. 1982). For OZ Gem, the mass loss rate is reported as $6 \times 10^{-6}\,M_\odot\,\mathrm{yr}^{-1}$ using a model of the IR emission from spherically symmetric circumstellar dust shells (Schutte & Tielens 1989). Therefore, the reddening is caused by the envelope mass ejected by the large mass loss: OZ Gem has been losing its envelope mass by mass loss at a rate much larger than the decrease rate of the envelope mass by the growth of the core through hydrogen shell burning of $dM_c/dt = L_H/(X_H E_H) = 8.8 \times 10^{-8} M_\odot \mathrm{yr}^{-1}$ at $\log(L/L_\odot) = 3.76 \pm 0.13$, where X_H and E_H are the hydrogen abundance and the nuclear energy release per unit mass of hydrogen, respectively. Note that there was no correction for the dimming effect of the star affected by interstellar extinction because OZ Gem is near the Earth.

We compared the P–L relation of the LMC with OZ Gem. Figure 9 shows the P–L diagram of the Mira variables in the LMC using the 2MASS catalog and OGLE-III as the same as Ita and Matsunaga (2011). The Mira variables were classified as C-rich (gray triangles) and O-rich stars (represented by x symbols) in the LMC by Soszyński et al. (2009). The prominent features of the P–L relation include a linear increase in M_K with increasing pulsation period (log P) for the O-rich Mira variables. In contrast, the dimming in M_K for the C-rich counterparts with a long pulsation period can be seen in figure 9. OZ Gem is found among the C-rich Mira variables. These C-rich stars also have reddened NIR colors (shown in figure 8) due to circumstellar dust and large mass loss (as discussed in Ita & Matsunaga 2011), like OZ Gem. Comparing NIR color

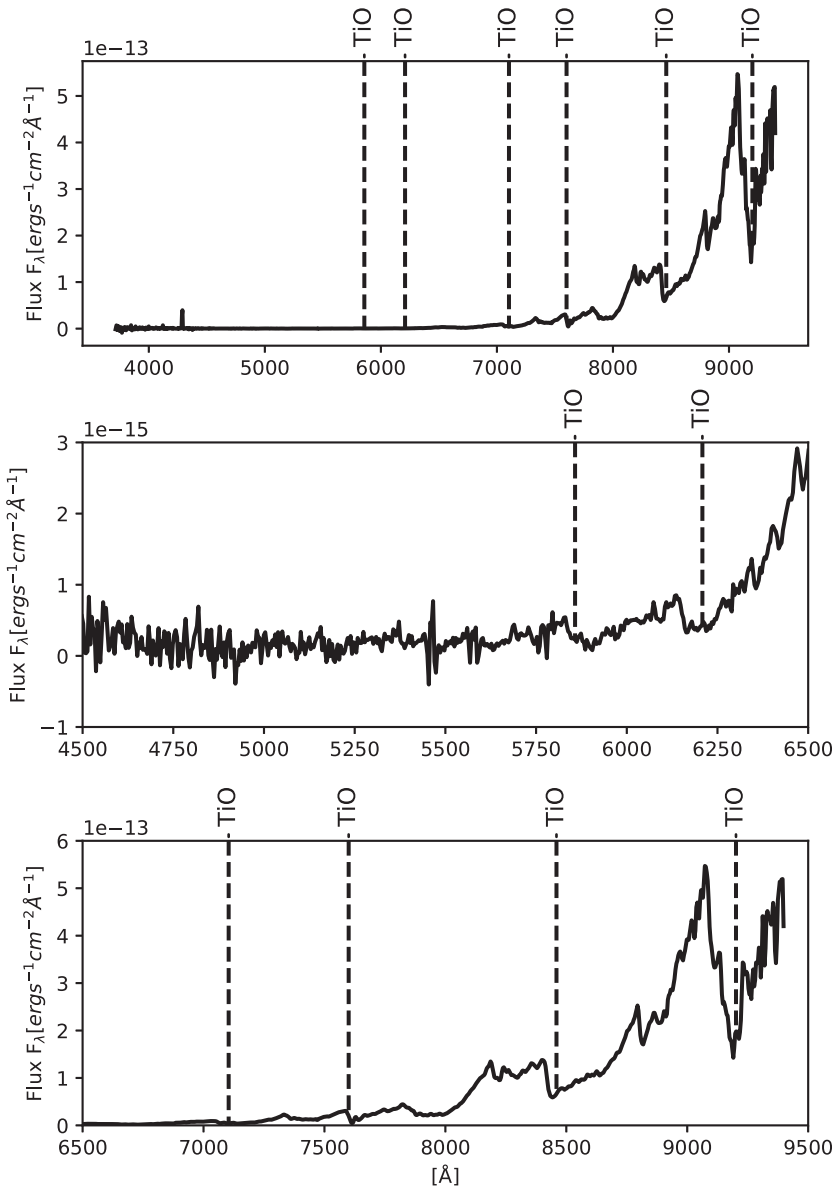

Fig. 7. Top panel: Full OZ Gem spectra showing the presence of multiple TiO absorption features. Middle and bottom panels: Zoomed parts of the full spectra.

and P–L relationship position, OZ Gem behaves like C-rich Miras.

4.3 The mass range and evolutionary status of OZ Gem

Generally, the Mira variables are classified by their O-rich or C-rich surface chemistry. The changes in the chemistry are caused by the third dredge-up (TDU) and also the hot-bottom burning during the thermal pulsating (TP) AGB evolution, the efficiencies of which are strongly dependent on the stellar mass. The star starts the evolution of the AGB phase with the helium shell burning as an M-type (O-rich) giant (the early AGB phase). After that, the AGB star undergoes hydrogen and helium shell burning alternately, attended by the helium shell flash (TP-AGB phase), during which the star decreases its envelope mass through the shell burning and also mass loss. The star is deprived from the envelope through mass loss at a rate greatly exceeding the growth rate of the core by the hydrogen burning, and eventually it leaves the giant branch (post-AGB phase) to end as a white dwarf. During the TP-AGB phase, AGB stars experience the TDU, which carries the nuclear products, especially carbon, away from the site of the helium flash convection up to the surface. The mass of stars a lower bound, $M_{\rm TDU}$, in order that the TDU may to accompany thermal pulses since the surface convection tends to be shallower for smaller luminosity. As the luminosity increases,

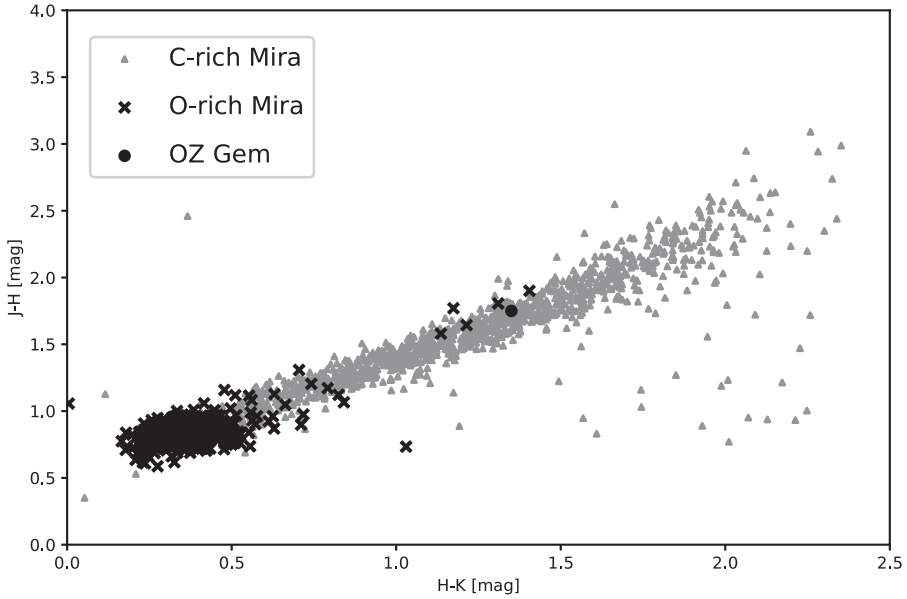

Fig. 8. Near-infrared color–color diagram of C-rich Mira and O-rich Mira in the LMC with OZ Gem. Circle: OZ Gem; triangle: C-rich Miras; cross: O-rich Miras.

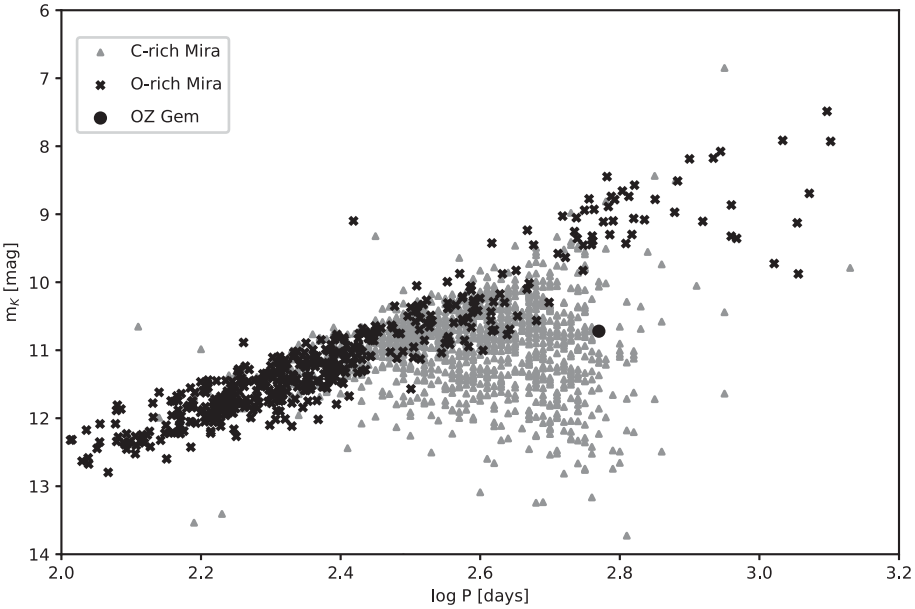

Fig. 9. P–L relation of C-rich (gray filled triangles) and O-rich (cross) Mira variables in the LMC. OZ Gem is represented by the black filled circle.

the surface convection deepens to raise the temperature in the bottom. If the temperature rises high enough, the CN cycle reactions operate in the bottom and convert the carbon dredged up by TDU to nitrogen in the surface convection (hot-bottom burning: HBB). This occurs in AGB stars of initial mass greater than the threshold mass, $M_{\rm HBB}$, since the luminosity reach higher for a larger initial mass. The resultant surface chemistry differs according to the initial mass, $M_{\rm i}$, of the star, and is divided into three cases according to the occurrence of TDU and HBB:

(1) Very low-mass AGB stars with $M_{\rm i} < M_{\rm TDU}$ get through the TP-AGB without experiencing the TDU, and hence keep the O-rich surface abundance.
(2) Low-mass AGB stars in the range of $M_{\rm TDU} \leq M_{\rm i} < M_{\rm HBB}$ dredge up the carbon produced in the He shell, and eventually the surface abundance changes from O-rich to C-rich when the carbon exceeds the oxygen in number (C/O $>$ 1) in the envelope.
(3) Massive AGB stars with $M_{\rm i} > M_{\rm HBB}$ undergo HBB, which prevents the surface chemistry from changing

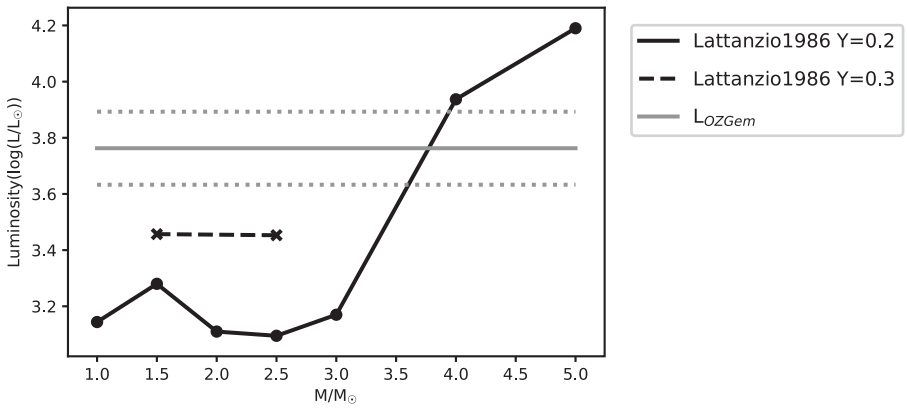

Fig. 10. L–M diagram of AGB star derived from table 8 of Lattanzio (1986). Black circle and solid line: mass–luminosity relation in helium abundance $Y = 0.2$. Cross and dashed line: Mass–luminosity relation in helium abundance $Y = 0.3$. Gray solid line: luminosity of OZ Gem. Gray dotted line: error in luminosity.

from O-rich to C-rich despite the dredge-up of carbon.

The threshold masses are estimated at $M_{\rm TDU} \simeq 1.5$–$2.2\,M_\odot$ and $M_{\rm HBB} \simeq 3.5$–$4.5\,M_\odot$ for the solar metallicities from the evolution models (Lattanzio 1989; Karakas 2010; Ventura et al. 2018), though the precise values are subject to uncertainties, especially that of the numerical prescription for the convective mixing, and are also dependent on the metallicity of the stars.

Figure 10 shows the luminosity at the stage when the star evolves into the first major thermal pulse as a function of the initial mass, by taking evolutionary models from Lattanzio (1986). From this figure, we may read off the initial mass of the stars which would arrive at the onset of the TP-AGB phase with the same luminosity as observed from OZ Gem at $M_{\rm TP} = 3.8 \pm 0.2\,M_\odot$ for $Y = 0.2$. Since the luminosity may increase with the helium abundance, $M_{\rm TP}$ could be smaller for the solar helium abundance ($Y = 0.25$), and yet the difference is small because of the steep gradient, $d\log L/dM_{\rm i}$, for $M_{\rm i} = 3$–$4\,M_\odot$. Our results from the spectroscopy as well as some masers (H_2O, SiO, OH) provide evidence that OZ Gem is an O-rich star. Then, we have two ranges of the initial mass that allow the star to retain the O-rich chemistry until it evolves to attain the observed luminosity of OZ Gem, one being $M_{\rm i} < M_{\rm TDU}$ and the other $M_i > \min\{M_{\rm TP}, M_{\rm HBB}\}$. The stars with an initial mass in the range $M_{\rm TDU} \le M_i \le \min\{M_{\rm TP}, M_{\rm HBB}\}$ change their surface abundance into C-rich before attaining the observed luminosity of OZ Gem.

We consider possible scenarios to explain the O-richness of OZ Gem. The first is the star with a very low initial mass. In this case, OZ Gem is now thermal pulsating and is likely to end its life as O-rich because of the mass loss at a much larger rate than the growth rate of the core by hydrogen shell burning. In the Galaxy, there are a number of OH/IR stars with a relatively short period like OZ Gem (Jiménez-Esteban et al. 2006). On the other hand, in the LMC, O-rich Miras are scarcely observed near the location of OZ Gem on the P–L diagram, although pulsation periods, especially those of the fundamental mode, depend little on the metallicity (e.g., Trabucchi et al. 2019). Thus we have to seek a counterpart of OZ Gem among C-rich Miras in the LMC. This is consistent with the prediction of the evolution models that the low-mass limit to the TDU decreases for smaller metallicity, e.g., $M_{\rm TDU} = 2.25$ to $1.5M_\odot$ between the solar and LMC metallicities (e.g., Karakas 2010). In other words, we may determine the metallicity dependence of $M_{\rm TDU}$ by examining a difference between the Galaxy and the LMC in the distributions of C-rich and O-rich Miras.

The second is a massive star. In this case, OZ Gem has to remain in the earlier evolution stage, and hence the problem is that the effective temperature seems too high to explain such a large mass loss rate as estimated for OZ Gem. The mass loss is indispensable for explaining the observed period, since with a large initial mass, the period is too short unless the star has lost its envelope mass. On the other hand, massive stars have to survive heavy mass loss since they are expected to evolve through the TP-AGB phase to develop a C-rich surface abundance or to keep an O-rich surface abundance for $M_{\rm i} \ge M_{\rm HBB}$. The latter have relevance to OH/IR sources with $\log P \gtrsim 3$, whose counterparts are observed in the LMC as O-rich Miras with a long period of $\log P \sim 3$.

In addition, the different surface chemistry arises simply from the amount of dredged-up carbon necessary to change from O-rich to C-rich; for larger metallicity, a larger amount of carbon is necessary to convert from O-rich to C-rich abundance. This increases the duration of the O-rich phase and delays the change to C-rich surface chemistry in the Galactic AGB stars in comparison with those in

the LMC. This is compatible with the location of OZ Gem on the P–L diagram as compared with O-rich Miras in the LMC. But it also means that C-rich Miras in the Galaxy have to be distributed even with longer periods than OZ Gem. In contrast, we see that C-rich Miras of the LMC are scarcely observed with longer periods than OZ Gem, despite the lower metallicity, and hence lower efficiency of mass loss.

In summary, OZ Gem is likely to constitute a low-mass OH/IR star in the Milky Way galaxy. In addition, this is the first observational evidence that $M_{\rm TDU}$ exists and varies with the solar and LMC metallicity. Our observation result suggests that applying the P–L relation of the LMC to the Milky Way could be misleading.

It is likely that OZ Gem would have been misinterpreted as a C-rich star based on the LMC P–L relation and two-color diagram. This highlights the importance of the effort to derive the P–L relation of variable stars in the Milky Way.

4.4 OZ Gem position discrepancy

We found an offset of $(-1.6 \pm 3.0, -34.8 \pm 3.4)$ mas between the central position of the H_2O masers and the derived stellar position in Gaia DR2. There are two possible explanations for the observed offset between the VLBI H_2O maser data and Gaia: the three-dimensional maser kinematics and the stellar surface granulation pattern (Chiavassa et al. 2011).

The maser proper motions shown in figure 4 show a well-delineated red- and blue-shifted outward motion. If we consider this to be a spherically expanding shell, then the position of the driving source, OZ Gem, will be at the dynamical center of the expansion. However, we note that the H_2O masers are pumped under special conditions, and this could affect the observed symmetry in the distribution, thus affecting the derived dynamical center.

On the other hand, Chiavassa et al. (2009, 2010, 2011) reported that stars (especially red super-giants, RSGs) are characterized by vigorous convection resulting in a granulation pattern on the stellar surface. In RSGs, these granules can be irregular in pattern when observed in the optical bands and can be as large as a solar radius in size. In particular, RSGs give rise to large granules that are comparable to the stellar radius in the H and K' bands. This granulation results in brightening of different parts of the star at different times, and could change significantly over a few years, thus affecting the astrometric results of telescopes like Gaia. This effect, along with the $\sim$0.3 mas position error toward OZ Gem reported by Gaia (Gaia Collaboration 2018), may have contributed to the observed offset in our VLBI results as compared to Gaia. Even taking this effect into account, the offset cannot be explained. If the star positions from Gaia are accurate, the maser position is south of the star position. These biased maser distributions may be caused by anisotropic outflows of OZ Gem. Therefore, the distribution of water masers seems not to be necessarily spherically symmetric; consideration of a new geometry for the circumstellar environment is required.

5 Conclusion

The first VLBI annual parallax measurement toward the Mira variable star OZ Gem resulted in $\pi = 0.806 \pm 0.039$ mas, corresponding to a distance of $D = 1.24 \pm 0.06$ kpc. This has only 4.8% error. We also successfully derived the mean J-, H-, and K'-band magnitudes of OZ Gem to be 5.75 ± 0.47 mag, 4.00 ± 0.16 mag, and 2.65 ± 0.16 mag, respectively. The pulsation period of OZ Gem fitted with the K'-band magnitudes is 592 ± 1 d. This represents the first report of the pulsation period of OZ Gem.

Applying our results on OZ Gem to the known LMC P–R relation confirms the known fact that the Milky Way has a metallicity that is higher than the LMC. We confirmed OZ Gem to be an O-rich Mira star, while the LMC P–L relation suggested it should be a C-rich star.

Our results highlight the need to constrain the P–L relation of the Milky Way independently using variable stars from within it.

Acknowledgment

We thank the VERA staff for both operating the VERA telescope and helping us with the data reduction. JOC acknowledges support by the Italian Ministry of Foreign Affairs and International Cooperation (MAECI Grant Number ZA18GR02) and the South African Department of Science and Technology's National Research Foundation (DST-NRF Grant Number 113121) as part of the ISARP RADIOSKY2020 Joint Research Scheme.

References

Benson, P. J., Little-Marenin, I. R., Woods, T. C., Attridge, J. M., Blais, K. A., Rudolph, D. B., Rubiera, M. E., & Keefe, H. L. 1990, ApJS, 74, 911

Bessell, M. S., Castelli, F., & Plez, B. 1998, A&A, 333, 231

Buzzoni, A., Patelli, L., Bellazzini, M., Pecci, F. F., & Oliva, E. 2010, MNRAS, 403, 1592

Chiavassa, A., et al. 2011, A&A, 528, A120

Chiavassa, A., Haubois, X., Young, J. S., Plez, B., Josselin, E., Perrin, G., & Freytag, B. 2010, A&A, 515, A12

Chiavassa, A., Plez, B., Josselin, E., & Freytag, B. 2009, A&A, 506, 1351

Chikada, Y., Kawaguchi, N., Inoue, M., Morimoto, M., Kobayashi, H., & Mattori, S. 1991, in Frontiers of VLBI, ed. H. Hirabayashi et al. (Tokyo: Universal Academy Press), 79

Feast, M. W. 2009, in Proc. AGB Stars and Related Phenomena, ed. T. Ueta et al. (Tokyo: National Astronomical Observatory of Japan), 48
Feast, M. W., Glass, I. S., Whitelock, P. A., & Catchpole, R. M. 1989, MNRAS, 241, 375
Feast, M. W., Robertson, B. S. C., Catchpole, R. M., Evans, T. L., Glass, I. S., & Carter, B. S. 1982, MNRAS, 201, 439
Gaia Collaboration, 2018, A&A, 616, A1
Guglielmo, F., Epchtein, N., Arditti, F., & Sevre, F. 1997, A&AS, 122, 489
Honma, M., et al. 2008a, PASJ, 60, 935
Honma, M., et al. 2012, PASJ, 64, 136
Honma, M., Tamura, Y., & Reid, M. J. 2008b, PASJ, 60, 951
Ita, Y., et al. 2004, MNRAS, 347, 720
Ita, Y., & Matsunaga, N. 2011, MNRAS, 412, 2345
Jiménez-Esteban, F. M., García-Lario, P., Engels, D., & Manchado, A. 2006, A&A, 458, 533
Karakas, A. I. 2010, MNRAS, 403, 1413
Kawabata, K. S., et al. 2008, in Proc. SPIE, 7014, Ground-based and Airborne Instrumentation for Astronomy II, ed. I. S. McLean et al. (Bellingham, WA: SPIE), 70144L
Kim, J., Cho, S.-H., & Kim, S. J. 2013, AJ, 145, 22
Kim, J., Cho, S.-H., & Kim, S. J. 2014, AJ, 147, 22
Lattanzio, J. C. 1986, ApJ, 311, 708
Lattanzio, J. C. 1989, ApJ, 344, L25
Luck, R. E., Moffett, T. J., Barnes, T. G., & Gieren, W. P. 1998, AJ, 115, 605
Nagayama, T. 2016, in Proc. SPIE, 9912, Advances in Optical and Mechanical Technologies for Telescopes and Instrumentation II, ed. R. Navarro & J. H. Burge (Bellingham, WA: SPIE), 991237
Nakagawa, A., Kurayama, T., Matsui, M., Omodaka, T., Honma, M., Shibata, K. M., Sato, K., & Jike, T. 2016, PASJ, 68, 78
Niell, A. E. 1996, J. Geophys. Res., 101, 3227
Oyama, T., et al. 2016, PASJ, 68, 105
Pushkarev, A. B., & Kovalev, Y. Y. 2012, A&A, 544, A34
Reid, M. J., et al. 2014, ApJ, 783, 130
Schutte, W. A., & Tielens, A. G. G. M. 1989, ApJ, 343, 369
Solf, J. 1978, A&AS, 34, 409
Soszyński, I., et al. 2009, Acta Astron., 59, 335
Torres, G. 2010, AJ, 140, 1158
Trabucchi, M., Wood, P. R., Montalbán, J., Marigo, P., Pastorelli, G., & Girardi, L. 2019, MNRAS, 482, 929
van Leeuwen, F. 2007, A&A, 474, 653
Ventura, P., Karakas, A., Dell'Agli, F., García-Hernández, D. A., & Guzman-Ramirez, L. 2018, MNRAS, 475, 2282
Zuckerman, B., & Lo, K. Y. 1987, A&A, 173, 263